Noncubic local distortions and spin-orbit excitons in K_2IrCl_6

Seungyeol Lee,[1] Beom Hyun Kim,[2,*] Maeng-Je Seong,[1,†] and Kwang-Yong Choi[3,‡]
[1]*Department of Physics, Chung-Ang University, Seoul 06974, Republic of Korea*
[2]*Korea Institute for Advanced Study, Seoul 02455, Republic of Korea*
[3]*Department of Physics, Sungkyunkwan University, Suwon 16419, Republic of Korea*

(Received 10 March 2022; revised 13 May 2022; accepted 16 May 2022; published 31 May 2022)

The cubic antifluorite K_2IrCl_6 has recently garnered renewed attention due to its relevance to Kitaev magnetism. Combining Raman spectroscopy with numerical calculations, we investigate its electronic structure and ensuing low-lying excitations as well as lattice instabilities. For temperatures below $T^* \approx 180$ K, we observe several lattice anomalies: (i) a gradual appearance of the symmetry-forbidden phonons; (ii) a central-mode-like excitation; and (iii) a soft-mode-like behavior of the Γ^{5+} mode involving vibrations of the K^+ ion relative to the Cl^- ion. All these features indicate the occurrence of local noncubic distortions. At high energies, we observe spin-orbit (SO) excitons made of five peaks at $\omega = 0.62$–0.79 eV as well as a weak electronic excitation at $\omega = 0.12$–0.86 eV. Our numerical calculations reproduce their spectral energy and shape with the electronic parameters: SO coupling $\lambda = 465$ meV; Hund's coupling $J_H = 300$ meV; tetragonal distortion strength $\Delta_t = 30$ meV and on-site Coulomb interaction $U = 2.2$ eV. The multiple SO excitons are interpreted in terms of bounded SO excitons of the $|j_{\text{eff}} = \frac{3}{2}, \pm\frac{1}{2}\rangle$ states arising from the coupling between the SO excitons and electron-hole excitations. Our results showcase that K_2IrCl_6 is on the brink of a structural phase transition.

DOI: 10.1103/PhysRevB.105.184433

I. INTRODUCTION

Over the last decade, half-filled $4d$ and $5d$ transition-metal (TM) compounds have been a topic of keen interest as a material platform for realizing novel quantum ground states. A concerted interplay of on-site Coulomb repulsion, crystal field splitting, and spin-orbit (SO) coupling with comparable energy scales engenders $j_{\text{eff}} = 1/2$ SO-assisted Mott insulators and constitutes a prerequisite for Kitaev magnetism [1–8].

The prominent classes of materials encompass honeycomb iridates A_2IrO_3 (A = Li, Na) and their derivatives and α-$RuCl_3$, which are proximate to Kitaev spin liquids entailing Majorana fermions [7–13]. Recently, searching for Kitaev materials has expanded into triangular, kagome, pyrochlore, hyperkagome, and face-centered-cubic (fcc) lattice systems beyond the d^5 $j_{\text{eff}} = 1/2$ honeycomb lattice [14–19]. In these magnetic sublattices built on edge-sharing octahedra, the $j_{\text{eff}} = 1/2$ Ir^{4+} ions are predicted to accommodate bond-directional Kitaev interactions and host exotic states of matter including vortex crystal, spin-liquid, and nematic states.

In the pursuit of fcc Kitaev physics, a renewed interest in a family of cubic antifluorite-type A_2MX_6 (A = alkali metals; M = $4d/5d$ TM; X = halides) has arisen. In the early days, the magnetism of A_2MX_6 was described within an antiferromagnetic Heisenberg model on the frustrated fcc lattice [20–31]. However, recent theoretical and experimental studies unraveled that a parallel edge-sharing geometry of isolated MX_6 octahedra (M-X-X-M superexchange pathways) provided an alternative route to achieve bond-directional Kitaev exchange interactions beyond the Jackeli and Khaliullin mechanism based on direct edge-sharing IrO_6 octahedra in A_2IrO_3 [32,33].

Here, we will focus our attention on the fcc antiferromagnet K_2IrCl_6, which crystallizes in the $Fm\bar{3}m$ space group. Unlike other A_2MX_6 antifluorite compounds, K_2IrCl_6 experiences neither global nor local symmetry lowering down to at least 0.3 K [34,35]. The ideal antifluorite structure ensures that a near-ideal $j_{\text{eff}} = 1/2$ electronic state of the Ir^{4+} ions is retained over the entire temperature range. Notwithstanding, the unavoidable, weak noncubic crystal-field splitting of $\Delta \approx 70$ meV is attributed to the enhanced covalency of the Ir and Cl bonds, which, in turn, leads to the reduction of the $g = 1.79(1)$ factor from the free-spin value of $g = 2$ [36]. As possible origins of the deviations from a perfect $j_{\text{eff}} = 1/2$ state, local structural distortions or a dynamic Jahn-Teller effect are invoked.

Ab initio calculations advocate the presence of a sizable antiferromagnetic Kitaev exchange interaction of $K/k_B \simeq 5$ K in addition to a dominant nearest-neighbor Heisenberg interaction of $J_1/k_B \simeq 13$ K and a weak next-nearest-neighbor exchange interaction of $J_2/k_B \simeq 0.2$ K [34]. These magnetic parameters can explain a type-III antiferromagnetic order at $T_N \approx 3$ K. Contrarily, a subsequent study of antiferromagnetic resonance modes reveals a much smaller value of $K/k_B \simeq 1$ K, alluding to the significance of Hund's coupling on the Cl ligand [36]. Given that K_2IrCl_6 is on the verge of structural instabilities, electronic and lattice excitations should be simultaneously assessed for a better understanding of an electronic structure and SO-entangled state.

*bomisu@kias.re.kr
†mseong@cau.ac.kr
‡choisky99@skku.edu

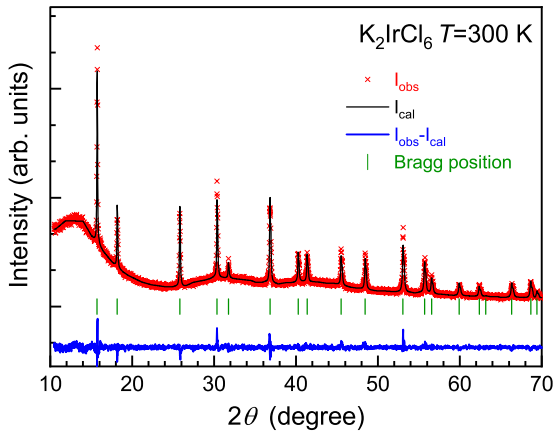

FIG. 1. X-ray diffraction pattern of K_2IrCl_6 samples. The observed data, Rietveld refinement fit, Bragg peaks, and difference curve are denoted by the cross symbols, black solid line, green bars, and blue line, respectively.

In this study, we combine Raman spectroscopy with exact diagonalization calculations to probe and quantify low-energy phonon and electronic excitations of K_2IrCl_6. Phonon excitations reveal noncubic local distortions. Multiple SO excitations evince their bounded nature through their coupling to electron-hole excitations. Further, we find that incipient structural instability affects an electronic structure to some degree.

II. EXPERIMENTAL DETAILS

Commercially available K_2IrCl_6 powders (99.99% purity, Alfa Aesar) were dissolved in distilled water using a glass beaker. The supersaturated solution was then heated up to 90 °C and kept at the temperature for 10 h. After cooling the solution down to room temperature at a rate of 1.25 °C/h, black, octahedral-shaped crystals of K_2IrCl_6 with a diameter of 1–2 mm were obtained. A single crystallinity of the obtained samples was analyzed and confirmed using an x-ray diffractometer (D8-Advance, Bruker-AXS), and a Laue diffractometer. In Fig. 1, we plot the room-temperature powder x-ray diffraction pattern of K_2IrCl_6 together with Rietveld refinements. The K_2IrCl_6 compound crystallizes in the $Fm\bar{3}m$ space group with the fitted lattice parameters $a = b = c = 9.75479(0)$ Å ($\chi^2 = 1.62$), which are in good agreement with previous results [34,35].

Polarization-resolved Raman spectroscopic measurements were carried out using a micro-Raman spectrometer (XperRam200VN, NanoBase) and a holographic transmission diffraction grating (1800 grooves/mm). The samples were shined with a diode-pumped-solid-state (DPSS) laser of wavelength $\lambda = 532$ nm. The laser beam was focused on a few-micrometer-diameter spot on the surface of the crystals using a $\times 40$ microscope objective. To reduce local heating effects, the incident laser power was set below $P = 100$ μW. We further employed a notch filter to reject Rayleigh scattering to a lower cutoff frequency of 15 cm^{-1}. For temperature-dependent Raman experiments, single crystals of K_2IrCl_6 were mounted onto a liquid-He-cooled continuous flow cryostat (MicrostatHires, Oxford) by varying a temperature $T = 4.3$–390 K.

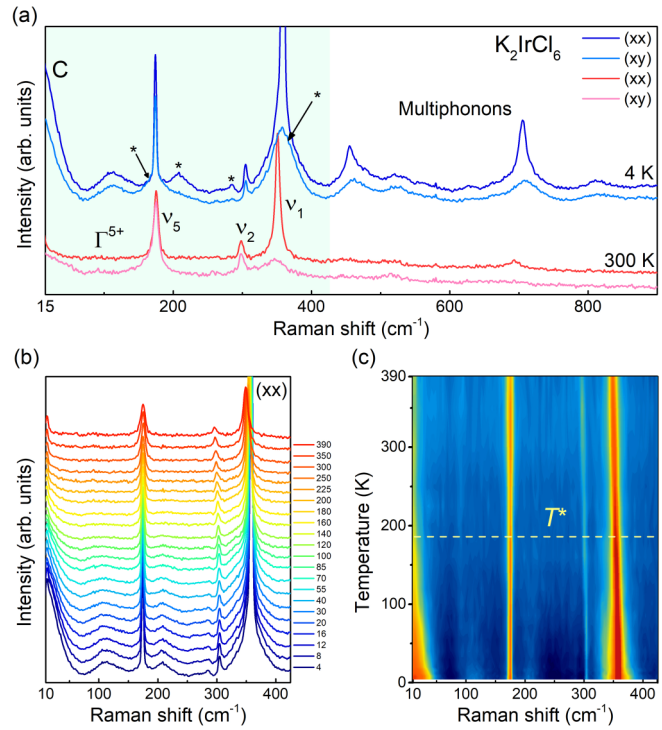

FIG. 2. (a) Raman spectra of K_2IrCl_6 measured at $T = 4$ K and 300 K in parallel (blue and red lines) and cross (light blue and pink) polarizations. C near zero shift denotes a central-mode-like excitation and the asterisks label activated phonon modes at low temperatures. The Γ^{5+} and $\nu_i (i = 1, 2, 5)$ modes are symmetry-allowed phonons for the fcc phase. The color shading differentiates one-phonon from multiphonon scatterings. (b) Temperature dependence of one-phonon Raman spectra in parallel polarization. The spectra are vertically shifted by a constant amount. (c) Contour plot of the one-phonon intensities in the temperature-Raman-shift plane. The horizontal dotted line represents a characteristic temperature, at which the phonon intensity starts to increase strongly.

To analyze the Raman spectra involving SO excitations theoretically, we employed the Hubbard model of t_{2g} orbitals incorporating SO coupling, tetragonal distortion, Kanamori-type Coulomb interaction, and hopping integrals. We considered the five Ir sites in the xy-plane to simulate Raman-active electronic excitations in the (xx) and (xy) polarization channels [see the inset of Fig. 5(b)]. We set the on-site Coulomb repulsion U and Hund's exchange J_H to be 2.2 and 0.3 eV, respectively, according to Ref. [34]. Hopping integrals characterized by the four parameters (t_1, t_2, t_3, t_4) were set with scaled values of those in Ref. [34]. The optimal scale of hopping integrals (s), the SO coupling (λ), and the tetragonal distortion strengths (Δ_t) were set to reproduce experimental Raman spectra. We calculated the Raman spectra by solving the Kramers-Heisenberg-Dirac formula for Stock's scattering (see the details in the Appendix).

III. RESULTS AND DISCUSSION

A. Phonon excitations and central mode

In Fig. 2, we present the polarized Raman spectra of K_2IrCl_6 measured at base ($T = 4$ K) and room temperature

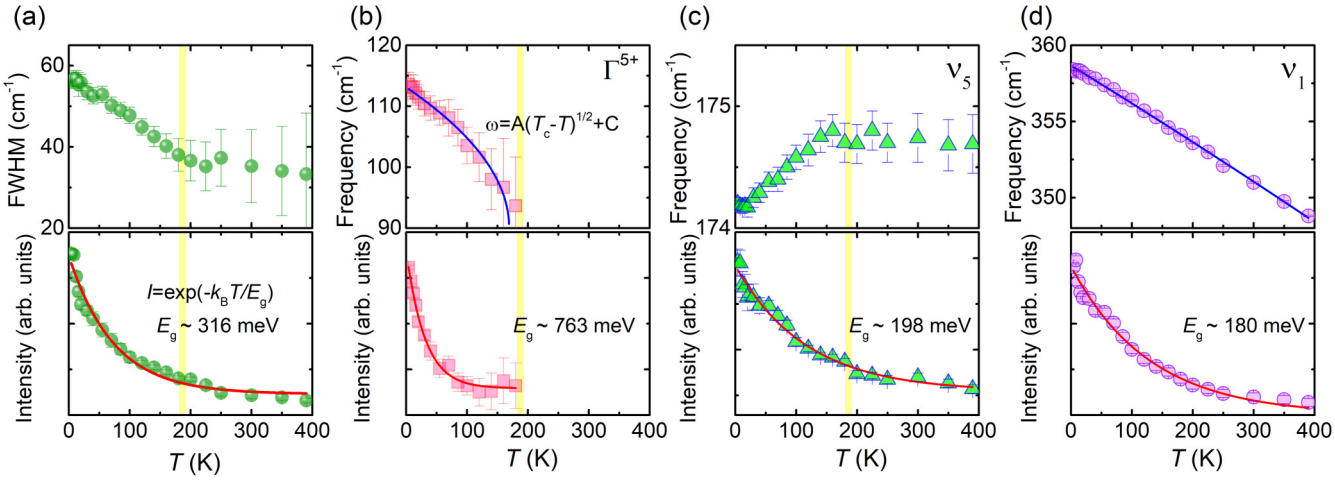

FIG. 3. Temperature dependence of the full width at half maximum (FWHM) $\Gamma(T)$ and intensity $I(T)$ for (a) the quasielastic scattering C. (b) Thermal evolution of the frequency $\omega(T)$ and $I(T)$ for (b) the Γ^{5+} mode, (c) the ν_5 mode, and (d) the ν_1 mode. The yellow vertical bars mark the characteristic temperature T^*. $\omega(T)$ of the Γ^{5+} mode is described by the mean-field-like behavior $\omega(T) = A(T^* - T)^{1/2} + \omega_0$ and $\omega(T)$ of the ν_1 mode is fitted to an anharmonic model $\omega(T) = \omega_0 + A[1 + 2/(e^{\hbar\omega/k_B T} - 1)]$. An exponentially decaying intensity $I(T)$ is modeled as $I(T) \propto \exp(-k_B T/E_g)$.

($T = 300$ K). Raman measurements were performed in two in-plane polarizations, namely, parallel (xx) and cross (xy) polarizations. Here, x is chosen to be an arbitrary direction in the crystallographic ab plane and y is rotated in plane by 90° with respect to x. In these scattering configurations, the factor group analysis for the $Fm\bar{3}m$ crystal symmetry yields the total irreducible representation for four Raman-active modes: $\Gamma = A_{1g}(xx, xy) + E_g(xx, xy) + 2T_{2g}(xx)$.

At room temperature, we were able to observe four one-phonon peaks in the frequency range of 10–400 cm^{-1} (marked by the color shading): one Γ^{5+} mode at 89 cm^{-1} and three internal modes at $\nu_5 = 174$ cm^{-1}, $\nu_2 = 299$ cm^{-1}, and $\nu_1 = 350$ cm^{-1} (refer to Ref. [37] for the notation). The weak Γ^{5+} mode corresponds to out-of-phase motions of the K atoms and the internal ν_i modes involve breathing and bending vibrations of the $IrCl_6$ octahedra. The weak structures appearing above 400 cm^{-1} are ascribed to multiphonon excitations. Overall, the observed room-temperature phonon peaks agree well with the factor group predictions for the undistorted fcc phase. At low temperature, on the other hand, we identify several new peaks as sidebands of the symmetry-allowed modes (marked by the asterisks) and quasielastic scattering (denoted by C). Noteworthy is that the newly activated excitations are considerably broader than the major phonon modes inherent to the fcc phase. Possibly, several unresolved peaks may coalesce or overlap.

Shown in Figs. 2(b) and 2(c) are the temperature variation of the one-phonon spectra and the color plot of the phonon intensity in the temperature-Raman-shift plane, respectively. As the temperature is lowered to the base temperature, the phonon intensities increase steadily with no apparent saturation. The continuous growth of the symmetry-forbidden phonons with decreasing temperature indicates the gradual development of local lattice distortions, rendering silent or infrared-active modes Raman-active.

We recall that many of A_2MX_6 antifluorite compounds display structural phase transitions driven by a soft rotational mode at the zone center (Γ) and zone boundary (X) [37,38]. In distorted fcc phases accompanying the tilt and rotation of the MX_6 octahedra and lattice deformations, phonon anomalies typical for the displacive-type phase transitions appear, including phonon sidebands, soft rotary modes, and a central mode. For the case of K_2IrCl_6, there are opposing experimental reports on the existence of symmetry-lowering structural transitions. An earlier study proposed a structural transition at $T_S = 2.8$ K [29]. In sharp contrast, very recent neutron powder diffraction and synchrotron x-ray diffraction measurements found no deviations from the ideal antifluorite structure down to 0.3 K [34,35]. However, the lacking structural transition seems to be incompatible with the splitting of the $j_{\text{eff}} = 3/2$ quartet into two doublets probed by resonant inelastic x-ray scattering (RIXS). As possible origins of the noncubic crystal-field splitting, local, static structural distortions and a dynamic Jahn-Teller effect are invoked. The present Raman data indicate that the noncubic local distortions develop in a continuous manner down to the lowest measured temperature, defying the occurrence of global structural transitions (*vide infra*).

We now turn to a thermal evolution of the phonon parameters extracted from fitting the phonon spectra to a sum of the Lorentzian profiles. In Fig. 3, we present the temperature dependence of the frequency $\omega(T)$, full width at half maximum (FWHM) $\Gamma(T)$, and intensity $I(T)$ for the four selected modes. Several salient features are discernible.

First, with decreasing temperature, the high-energy internal ν_1 mode exhibits a moderate hardening by 10 cm^{-1} and a narrowing, which can be described by an anharmonic model [see the solid line in Fig. 3(d)]. Notably, the integrated intensity shows a marked exponential-like decrease $I(T) \propto \exp(-k_B T/E_g)$. In insulating materials, the phonon intensity $I(T)$ hinges on changes in the electronic band energies caused by ionic displacements. Given the variation of penetration depth and scattering volume with temperature exerts minor effects, the steep increase of $I(T)$ alludes to the thermal modulation of electronic bands. Second, the ν_5

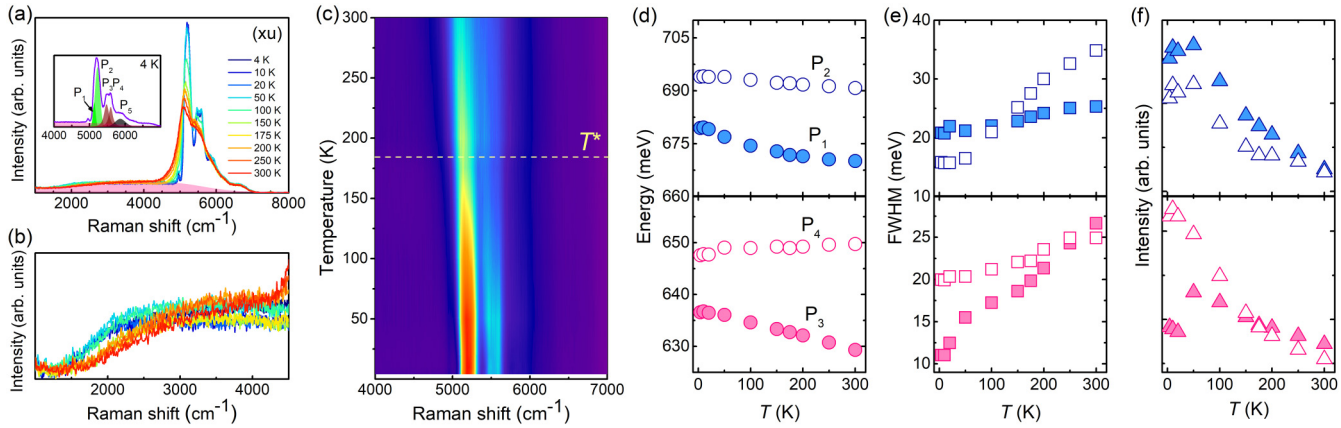

FIG. 4. (a) Temperature dependence of spin-orbit exciton and electronic (pink shading) excitations in (*xu*) polarization. The inset shows representative fit of the $T = 4$ K high-energy spectrum to five Lorentzian profiles $P_i (i = 1–5)$. (b) Enlarged view of a temperature evolution of the weak electron excitation in the frequency range of $\omega = 1000–4500$ cm^{-1}. (c) False-color map of the Raman intensity in the frequency-temperature plane. Temperature dependence (d) frequency, (e) FWHM, and (f) integrated intensity of the spin-orbit excitons P_i ($i = 1–4$).

mode exhibits a small softening below $T^* \approx 180$ K, indicative of the renormalization of phonon energy by magnetoelastic coupling or couplings to other degrees of freedom. Similar to the ν_1 mode, the phonon intensity increases exponentially with temperature. Third, the Γ^{5+} mode exhibits the most drastic temperature variation of $\omega(T)$ and $I(T)$. The rapid suppression of the Γ^{5+} signal above T^* disallows keeping track of the phonon parameters over the entire temperature range. We further note that the Γ^{5+} mode is much broader than the other symmetry-allowed modes. Most probably, the Γ^{5+} mode is intertangled with several symmetry-forbidden peaks, which do not permit an unambiguous decomposition. The giant frequency hardening by 20 cm^{-1} is largely approximated by the mean-field formula $\omega(T) = A(T^* - T)^{1/2} + \omega_0$. The soft-mode-like behavior of the Γ^{5+} mode suggests that the changing position of the K^+ ions relative to the Cl^- ion plays a pivotal role in the noncubic lattice distortions. Fourth, on cooling through T^*, the rather broad quasielastic scattering grows in intensity, which resembles a central mode expected in a displacive, second-order structural phase transition [39,40]. Generically, the central peak arises from the decay of a soft mode into acoustic modes or phonon density fluctuations. As such, the central peak becomes most intense at T_S, whose intensity reflects a fluctuation of the order parameter. This is contrasted by the unsaturated growth of the central-mode-like excitation in K_2IrCl_6, negating the presence of a well-defined structural transition at finite temperature.

Further comments on the observed lattice anomalies are in order. First, we could not detect a rotary soft mode, which lies below 100 cm^{-1} [37]. This means that a degree of cooperative rotations of the $IrCl_6$ octahedra is insufficient to trigger a structural transition. Second, the characteristic temperature T^* is close to the structural phase transition temperature $T_S = 170$ K of the sister compound [34,35]. In this vein, T^* is associated with the onset of the local noncubic distortions. Third, the empirical energy gap extracted from the exponentially decaying intensity with increasing temperature ranges from 180 meV to 763 meV, which falls into the energy of electronic excitations [see the pink shading in Fig. 4(a)]. All in all, the present Raman data underpins the persistence of local noncubic distortions to the base temperature with no hint of a global structural transition.

B. Spin-orbit exciton

To shine a light on a Mott insulating $j_{\text{eff}} = 1/2$ state, we measured high-energy excitations up to 8000 cm^{-1} (= 984 meV). As shown in Fig. 4(a), we can resolve five peaks $A_i (i = 1–5)$ between energy transfers $\omega = 0.62–0.79$ eV [inset of Fig. 4(a)] and the broad, weak electronic excitation between $\omega = 0.12–0.86$ eV [pink shading in Fig. 4(a)]. It is worthwhile to note that both the P_i ($i = 1–2$) and P_i ($i = 3–4$) exhibit a double-peak structure. We assign the $\omega = 0.62–0.79$ eV features to a SO exciton, which corresponds to excitonic quasiparticle excitations between the SOC-split levels $j_{\text{eff}} = 1/2$ and $j_{\text{eff}} = 3/2$ [41]. The Raman peak energies are slightly larger than $\omega = 0.58–0.71$ eV extracted from RIXS due to the different underlying mechanisms between the Raman scattering and RIXS [34,35]. As the peak energy is related to the SOC constant $\lambda_R \approx (2/3)\omega_{P_i}$, the SOC constant is evaluated to $\lambda_R \approx 0.41$ eV.

On heating, the SO excitons soften gradually and their scattering intensity is strongly reduced through T^*. We recall that a similar trend is observed for the temperature dependence of the low-energy lattice excitations [compare Fig. 3 with Fig. 4(f)]. This signals that an electronic structure is affected by lattice distortions. The influence of the lattice distortions on the electronic excitation is further seen in the thermal redistribution of the electronic continuum [see Fig. 4(b)]. Five peaks are modeled using Lorentzian line shapes, as marked by color shadings in the inset of Fig. 4(a). Fitting results are summarized in Figs. 4(c)–4(f). The P_i peaks undergo a red-shift and thermal broadening with increasing temperature. Qualitatively, the marked decrease of the scattering intensity resembles the exponential-like decay of the phonon intensity [compare Fig. 3 with Fig. 4(f)]. The energy difference between the (P_1, P_2) and (P_3, P_4) peaks amounts to roughly 10–20 meV. The split peaks are reminiscent of the double-peak RIXS spectra with the noncubic crystal-field splitting of $\Delta = 48–58$ meV [34,35]. The similar spectral features of the

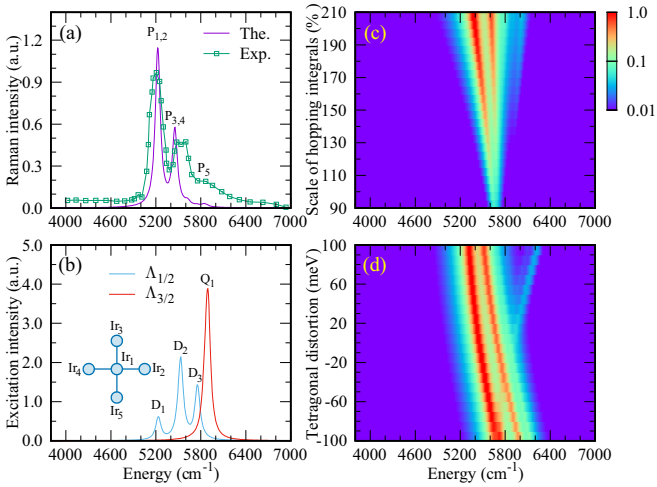

FIG. 5. (a) Comparison between the calculated Raman spectra (purple line) and experimental spin-orbital excitons (open green squares) in (xy) polarization. (b) The distribution functions $\Lambda_{1/2}$ and $\Lambda_{3/2}$ of single spin-orbit excitons for the $|j_{\rm eff} = \frac{3}{2}, \pm\frac{1}{2}\rangle$ and $|j_{\rm eff} = \frac{3}{2}, \pm\frac{3}{2}\rangle$ states, respectively. The inset depicts the schematic cluster configuration used for numerical calculations. The Raman spectrum map as a function of (c) the scale of hopping integrals and (d) the tetragonal distortion strength Δ_t. The density map is plotted on a logarithmic scale.

Raman and RIXS data support the notion that the $j_{\rm eff} = 3/2$ levels are split due to noncubic distortions. To examine this scenario, we performed numerical calculations.

Figure 5 presents the theoretical Raman spectra of the SO exciton. With the optimal hopping scale $s = 2$, the SO coupling strength $\lambda = 465$ meV, and the tetragonal distortion strength $\Delta_t = 30$ meV, we reach a good agreement between the theoretical (purple line) and experimental (green squares) Raman spectra as shown in Fig. 5(a). The adopted SO coupling strength is slightly larger than $\lambda_{\rm RIXS} \approx 444$ meV extracted by the RIXS data [35]. The calculated spectra comprise the two main peaks denoted as $P_{1,2} \approx 647.6$ meV (5223 cm^{-1}) and $P_{3,4} \approx 676.4$ meV (5456 cm^{-1}). Their peak positions coincide with the (P_1, P_2) and the (P_3, P_4) peaks in the experimental spectra, respectively. In addition, a weak peak appears around 724.4 meV (5843 cm^{-1}), which is located close to the P_5 peak.

To identify the origin of the observed multiple peaks, we examine the distribution of SO excitons. $\Lambda_{1/2}$ ($\Lambda_{3/2}$) is named the distribution of the SO exciton pertaining to the transition from $|j_{\rm eff} = \frac{1}{2}, \pm\frac{1}{2}\rangle$ to $|j_{\rm eff} = \frac{3}{2}, \pm\frac{1}{2}\rangle$ ($|j_{\rm eff} = \frac{3}{2}, \pm\frac{3}{2}\rangle$). As shown in Fig. 5(b), the distribution $\Lambda_{1/2}$ constitutes the three peaks denoted by D_1, D_2, and D_3, whereas the distribution $\Lambda_{3/2}$ consists of a single Q_1 peak. The peak positions of D_1, D_2, and Q_1 match well with those of the $P_{1,2}$, $P_{3,4}$, and P_5 peaks of the Raman spectra, respectively. Note that the hopping integral between the adjacent xy orbitals (t_3) is one order larger than others in the xy plane and that only $|j_{\rm eff} = \frac{3}{2}, \pm\frac{1}{2}\rangle$ spin-orbital states have an xy orbital component. We attribute the three-peak splitting of $\Lambda_{1/2}$ to the coupling between the SO excition and electron-hole excitations of the $j_{\rm eff} = 1/2$ orbitals. This coupling was proposed in Ir- and Ru-based honeycomb systems [42,43]. In K_2IrO_6, this scenario is probable since the electronic excitation [pink shading in Fig. 4(a)] overlaps with the SO excitations. In this conjecture, the $P_{1,2}$ and $P_{3,4}$ Raman peaks are related to the bounded SO excitons of the $|j_{\rm eff} = \frac{3}{2}, \pm\frac{1}{2}\rangle$ states. As plotted in Fig. 5(c), the $P_{1,2}$ and $P_{3,4}$ peaks of K_2IrO_6 shift to lower energies and their splitting slightly increases when the hopping scale increases. This behavior gives credence to the bounded SO exciton interpretation.

Figure 5(d) presents the Raman spectra as a function of the tetragonal distortion strength Δ_t. We find that the weak P_5 peak is well separated from the main $P_{1,2}$ and $P_{3,4}$ peaks for the positive Δ_t (elongated $IrCl_6$ octahedron). On the other hand, it is buried inside the main peaks for the negative Δ_t (contracted $IrCl_6$ octahedron). When Δ_t is set to about 30 meV, the experimental Raman peaks are well reproduced. Our calculations are consistent with the noncubic lattice distortion in K_2IrO_6.

IV. CONCLUSION

In summary, we elucidated the nature of structural instabilities K_2IrO_6 and multiple SO excitations. Our phonon data confirm noncubic local distortions, while lacking a true structural phase transition. We observe concomitantly multiple SO excitons and electronic excitations. The coupling between them raises the possibility of forming bounded SO excitons. Our results demonstrate that K_2IrO_6 has an incipient structural transition, which modifies slightly an electronic structure.

ACKNOWLEDGMENTS

This work was supported by the National Research Foundation (NRF) of Korea (Grant No. 2020R1A5A1016518). S.Y.L. was supported by a Chung-Ang University Graduate Research Scholarship in 2020. B.H.K. was supported by a KIAS Individual Grant (No. CG068702). Numerical computations have been performed with the Center for Advanced Computation Linux Cluster System at KIAS.

APPENDIX: NUMERICAL CALCULATION

We employ the Hubbard model of t_{2g} orbitals described by the following Hamiltonian:

$$
\begin{aligned}
H = & \sum_{i\alpha\sigma} \varepsilon_\alpha c^\dagger_{i\alpha\sigma} c_{i\alpha\sigma} + \lambda \sum_{i\alpha\beta\sigma\sigma'} (\mathbf{l}\cdot\mathbf{s})_{\alpha\sigma,\beta\sigma'} c^\dagger_{i\alpha\sigma} c_{i\beta\sigma'} \\
& + \frac{1}{2} \sum_{i,\sigma,\sigma',\alpha,\beta} U_{\alpha\beta} c^\dagger_{i\alpha\sigma} c^\dagger_{i\beta\sigma'} c_{i\beta\sigma'} c_{i\alpha\sigma} \\
& + \frac{1}{2} \sum_{i,\sigma,\sigma',\alpha\neq\beta} J_{\alpha\beta} c^\dagger_{i\alpha\sigma} c^\dagger_{i\beta\sigma'} c_{i\alpha\sigma'} c_{i\beta\sigma} \\
& + \frac{1}{2} \sum_{i,\sigma,\alpha\neq\beta} J'_{\alpha\beta} c^\dagger_{i\alpha\sigma} c^\dagger_{i\alpha\bar{\sigma}} c_{i\beta\bar{\sigma}} c_{\beta\sigma} \\
& + \sum_{\langle i,j\rangle\alpha\beta\sigma} \left(t^{\alpha\beta}_{ij} c^\dagger_{i\alpha\sigma} c_{j\beta\sigma} + \text{H.c.} \right), \qquad \text{(A1)}
\end{aligned}
$$

where $c^\dagger_{i\alpha\sigma}$ is the creation operator of t_{2g} electrons with α orbital and σ spin states at the ith site. The first term is the local electronic splitting due to the tetragonal distortion

($\varepsilon_{xy} = \frac{2\Delta_t}{3}$, $\varepsilon_{yz/zx} = -\frac{\Delta_t}{3}$). The second term gives the spin-orbit coupling of t_{2g} orbitals. The third, fourth, and fifth terms are associated with the Kanamori-type Coulomb interactions which are parameterized with the on-site Coulomb repulsion U and Hund's exchange J_H such that $U_{\alpha\alpha} = U$, $U_{\alpha\neq\beta} = U - 2J_{\rm H}$, and $J_{\alpha\beta} = J'_{\alpha\beta} = J_{\rm H}$. $t_{ij}^{\alpha\beta}$ are the hopping integrals between the nearest-neighboring α orbital at the i site and β orbital at the j site. In the xy plane, they are given as $t_{ij}^{yz,yz} = t_{ij}^{zx,zx} = t_1$, $t_{ij}^{yz,zx} = t_{ij}^{zx,yz} = t_2$, $t_{ij}^{xy,xy} = t_3$, and $t_{ij}^{xy,yz} = t_{ij}^{xy,zx} = t_{ij}^{yz,xy} = t_{ij}^{zx,xy} = t_4$.

To calculate the resonant Raman spectra, we solve the Kramers-Heisenberg-Dirac equation for the Stokes scattering as

$$I_{RM}(\omega, \boldsymbol{\epsilon}, \boldsymbol{\epsilon}') = \sum_f |M_{fg}(\boldsymbol{\epsilon}, \boldsymbol{\epsilon}')|^2 \delta(\omega - E_f + E_g), \quad \text{(A2)}$$

where

$$M_{fg}(\boldsymbol{\epsilon}, \boldsymbol{\epsilon}') = \langle \Psi_f | \boldsymbol{\epsilon}'^* \cdot \boldsymbol{j}^\dagger \frac{1}{\omega_{in} - H + E_g + i\delta_{in}} \boldsymbol{\epsilon} \cdot \boldsymbol{j} | \Psi_g \rangle, \quad \text{(A3)}$$

where $|\Psi_g\rangle$ ($|\Psi_f\rangle$) and E_g (E_f) are the ground (excited) state and its energy, respectively. $\boldsymbol{j}$ is the current operator of t_{2g} electrons, $\boldsymbol{\epsilon}$ ($\boldsymbol{\epsilon}'$) is the polarization vector of incident (scattered) photons, and ω_{in} and δ_{in} are the energy and broadening of an incident light.

To analyze the Raman spectra further, we calculate the distribution of single SO excitons. According to the authors of Ref. [41], the distribution of a single SO exciton at the ith site is given by

$$\Lambda_J^i(\omega) = -\frac{1}{\pi} \mathrm{Im} \sum_{\substack{m=\pm J \\ \sigma=\pm\frac{1}{2}}} \left\langle \Psi_{m\sigma}^i \right| \frac{1}{\omega - H + E_g + i\delta} \left| \Psi_{m\sigma}^i \right\rangle, \quad \text{(A4)}$$

where $|\Psi_{m\sigma}^i\rangle$ is the many-body state obtained by replacing a $|j_{\rm eff}^i = \frac{1}{2}, \sigma\rangle$ multiplet state ($\sigma = \pm\frac{1}{2}$) with a $|j_{\rm eff}^i = \frac{3}{2}, m\rangle$ multiplet state ($m = \pm\frac{1}{2}, \pm\frac{3}{2}$) at the ith site in the ground state ($|\Psi_{m\sigma}^i\rangle = |j_{\rm eff}^i = \frac{3}{2}, m\rangle\langle j_{\rm eff}^i = \frac{1}{2}, \sigma \mid \Psi_g\rangle$). m is either $\frac{1}{2}$ or $\frac{3}{2}$.

[1] W. Witczak-Krempa, G. Chen, Y.-B. Kim, and L. Balents, Ann. Rev. Condens. Matter Phys. **5**, 57 (2014).
[2] J. G. Rau, E. K.-H. Lee, and H.-Y. Kee, Ann. Rev. Condens. Matter Phys. **7**, 195 (2016).
[3] G. Cao and P. Schlottmann, Rep. Prog. Phys. **81**, 042502 (2018).
[4] B. J. Kim, H. Jin, S. J. Moon, J.-Y. Kim, B.-G. Park, C. S. Leem, J. Yu, T. W. Noh, C. Kim, S.-J. Oh, J.-H. Park, V. Durairaj, G. Cao, and E. Rotenberg, Phys. Rev. Lett. **101**, 076402 (2008).
[5] A. Y. Kitaev, Ann. Phys. (NY) **303**, 2 (2003).
[6] G. Jackeli and G. Khaliullin, Phys. Rev. Lett. **102**, 017205 (2009).
[7] S. M. Winter, A. A. Tsirlin, M. Daghofer, J. van den Brink, Y. Singh, P. Gegenwart, and R. Valentí, J. Phys.: Condens. Matter **29**, 493002 (2017).
[8] H. Takagi, T. Kakayama, G. Jackeli, G. Khaliullin, and S. E. Nagler, Nat. Rev. Phys. **1**, 264 (2019).
[9] Y. Singh and P. Gegenwart, Phys. Rev. B **82**, 064412 (2010).
[10] A. Glamazda, P. Lemmens, S.-H. Do, Y. S. Choi, and K.-Y. Choi, Nat. Commun. **7**, 12286 (2016).
[11] K. W. Plumb, J. P. Clancy, L. J. Sandilands, V. V. Shankar, Y. F. Hu, K. S. Burch, H.-Y. Kee, and Y.-J. Kim, Phys. Rev. B **90**, 041112(R) (2014).
[12] S.-H. Do, S.-Y. Kwon, D. T. Park, J. Yoshitake, J. Voneshen, Y. Motome, Y. S. Kwon, D. T. Adroja, D. J. Voneshen, K. Kim, T.-H. Jang, J.-H. Park, K.-Y. Choi, and S. Ji, Nat. Phys. **13**, 1079 (2017).
[13] D. Wulferding, Y. S. Choi, S.-H. Do, C. H. Lee, P. Lemmens, C. Faugeras, Y. Gallais, and K.-Y. Choi, Nat. Commun. **11**, 1603 (2020).
[14] I. Kimchi and A. Vishwanath, Phys. Rev. B **89**, 014414 (2014).
[15] A. M. Cook, S. Matern, C. Hickey, A. A. Aczel, and A. Paramekanti, Phys. Rev. B **92**, 020417(R) (2015).
[16] M. Becker, M. Hermanns, B. Bauer, M. Garst, and S. Trebst, Phys. Rev. B **91**, 155135 (2015).
[17] A. Catuneanu, J. G. Rau, H.-S. Kim, and H.-Y. Kee, Phys. Rev. B **92**, 165108 (2015).
[18] K. Li, S.-L. Yu, and J.-X. Li, New J. Phys. **17**, 043032 (2015).
[19] K. Shinjo, S. Sota, S. Yunoki, K. Totsuka, and T. Tohyama, J. Phys. Soc. Jpn. **85**, 114710 (2016).
[20] J. H. E. Griffiths and J. Owen, Proc. R. Soc. London Ser. A **226**, 96 (1954).
[21] J. H. E. Griffiths, J. Owen, J. G. Park, and M. F. Partridge, Proc. R. Soc. London Ser. A **250**, 84 (1959).
[22] C. A. Bailey and P. L. Smith, Phys. Rev. **114**, 1010 (1959).
[23] A. H. Cooke, R. Lazenby, F. R. McKim, J. Owen, and W. P. Wolf, Proc. R. Soc. London Ser. A **250**, 97 (1959).
[24] E. A. Harris and J. Owen, Proc. R. Soc. London Ser. A **289**, 122 (1965).
[25] M. T. Hutchings and C. G. Windsor, Proc. Phys. Soc. **91**, 928 (1967).
[26] V. J. Minkiewicz, G. Shirane, B. C. Frazer, R. G. Wheeler, and P. B. Dorain, J. Phys. Chem. Solids **29**, 881 (1968).
[27] J. W. Lynn, G. Shirane, and M. Blume, Phys. Rev. Lett. **37**, 154 (1976).
[28] H. W. Willemsen, R. L. Armstrong, and P. P. M. Meincke, J. Low Temp. Phys. **26**, 299 (1977).
[29] D. Moses, M. Sutton, R. L. Armstrong, and P. P. M. Meincke, J. Low Temp. Phys. **36**, 587 (1979).
[30] R. L. Armstrong, Phys. Rep. **57**, 343 (1980).
[31] M. Meschke, S. Marquardt, and K. Siemensmeyer, J. Magn. Magn. Mater. **226-230**, 621 (2001).
[32] A. Revelli, C. C. Loo, D. Kiese, P. Becker, T. Frohlich, T. Lorenz, M. Moretti Sala, G. Monaco, F. L. Buessen, J. Attig, M. Hermanns, S. V. Streltsov, D. I. Khomskii, J. van den Brink, M. Braden, P. H. M. van Loosdrecht, S. Trebst, A. Paramekanti, and M. Gruninger, Phys. Rev. B **100**, 085139 (2019).
[33] T. Birol and K. Haule, Phys. Rev. Lett. **114**, 096403 (2015).

[34] N. Khan, D. Prishchenko, Y. Skourski, V. G. Mazurenko, and A. A. Tsirlin, Phys. Rev. B **99**, 144425 (2019).
[35] D. Reig-i-Plessis, T. A. Johnson, K. Lu, Q. Chen, J. P. C. Ruff, M. H. Upton, T. J. Williams, S. Calder, H. D. Zhou, J. P. Clancy, A. A. Aczel, and G. J. MacDougall, Phys. Rev. Materials **4**, 124407 (2020).
[36] L. Bhaskaran, A. N. Ponomaryov, J. Wosnitza, N. Khan, A. A. Tsirlin, M. E. Zhitomirsky, and S. A. Zvyagin, Phys. Rev. B **104**, 184404 (2021).
[37] G. P. O'Leary and R. G. Wheeler, Phys. Rev. B **1**, 4409 (1970).
[38] D. Mintz, R. L. Armstrong, B. M. Powell, and W. J. L. Buyers, Phys. Rev. B **19**, 448 (1979).
[39] K.-Y. Choi, Yu. G. Pashkevich, K. V. Lamonova, H. Kageyama, and Y. Ueda, and P. Lemmens, Phys. Rev. B **68**, 104418 (2003).
[40] V. L. Ginzburg, A. P. Levanyuk, and A. A. Sobyanin, Phys. Rep. **57**, 151 (1980).
[41] J.-H. Lee, Y. Choi, S.-H. Do, B. H. Kim, M.-J. Seong, and K.-Y. Choi, npj Quantum Mater. **6**, 43 (2021).
[42] B. H. Kim, G. Khaliullin, and B. I. Min, Phys. Rev. B **89**, 081109(R) (2014).
[43] B. H. Kim, T. Shirakawa, and S. Yunoki, Phys. Rev. Lett. **117**, 187201 (2016).